H_2O_2-responsive liposomal nanoprobe for photoacoustic inflammation imaging and tumor theranostics via in vivo chromogenic assay

Qian Chen[a], Chao Liang[a], Xiaoqi Sun[a], Jiawen Chen[a], Zhijuan Yang[a], He Zhao[b], Liangzhu Feng[a], and Zhuang Liu[a,1]

[a]Institute of Functional Nano & Soft Materials, Jiangsu Key Laboratory for Carbon-Based Functional Materials and Devices, Soochow University, Suzhou, Jiangsu 215123, China; and [b]Department of Pediatric Research, Children's Hospital of Soochow University, Suzhou, Jiangsu 215123, China

Edited by Hongjie Dai, Stanford University, Stanford, CA, and approved April 12, 2017 (received for review February 6, 2017)

Abnormal H_2O_2 levels are closely related to many diseases, including inflammation and cancers. Herein, we simultaneously load HRP and its substrate, 2,2′-azino-bis(3-ethylbenzothiazoline-6-sulfonic acid) (ABTS), into liposomal nanoparticles, obtaining a Lipo@HRP&ABTS optical nanoprobe for in vivo H_2O_2-responsive chromogenic assay with great specificity and sensitivity. In the presence of H_2O_2, colorless ABTS would be converted by HRP into the oxidized form with strong near-infrared (NIR) absorbance, enabling photoacoustic detection of H_2O_2 down to submicromolar concentrations. Using Lipo@HRP&ABTS as an H_2O_2-responsive nanoprobe, we could accurately detect the inflammation processes induced by LPS or bacterial infection in which H_2O_2 is generated. Meanwhile, upon systemic administration of this nanoprobe we realize in vivo photoacoustic imaging of small s.c. tumors (~2 mm in size) as well as orthotopic brain gliomas, by detecting H_2O_2 produced by tumor cells. Interestingly, local injection of Lipo@HRP&ABTS further enables differentiation of metastatic lymph nodes from those nonmetastatic ones, based on their difference in H_2O_2 contents. Moreover, using the H_2O_2-dependent strong NIR absorbance of Lipo@HRP&ABTS, tumor-specific photothermal therapy is also achieved. This work thus develops a sensitive H_2O_2-responsive optical nanoprobe useful not only for in vivo detection of inflammation but also for tumor-specific theranostic applications.

hydrogen peroxide | inflammation | tumor | photoacoustic imaging | photothermal therapy

Hydrogen peroxide (H_2O_2) plays an active role in various physiological processes including cell growth, immune response, and senescence (1, 2). An imbalance in H_2O_2 production is closely associated with diseases such as cancers, diabetes, inflammation, and cardiovascular and neurodegenerative diseases (3, 4). Therefore, the accurate and sensitive detection of H_2O_2 would have significant clinical value not only for disease diagnosis but also for better understanding of disease mechanisms. However, in vivo imaging of H_2O_2 for clinical applications remains a challenging task owing to the relatively low concentrations of H_2O_2 in physiological environments (below ~50 μM) (5, 6). Previously, boronate-based fluorescent probes have been explored for detection of physiologic H_2O_2 (with the detection limit at a few micromoles), relying on the H_2O_2-mediated transformation of arylboronates to phenols, generating fluorescence under visible light excitation (5–8). Moreover, a number of peroxalate-based nanoparticles have also been developed for in vivo H_2O_2-responsive bioluminescence imaging (9). However, the performance of in vivo H_2O_2 detection by either fluorescence or bioluminescence imaging is limited by the tissue penetration depth of those conventional optical imaging techniques, in particular with visible light used in those systems, hampering accurate detection of H_2O_2 in deep tissues (3, 9). Thus, it is necessary to design nanoprobes that allow accurate in vivo imaging of H_2O_2 in deep tissues with high specificity and sensitivity. In addition, it may be of great interest to realize H_2O_2-specific treatment to fight certain types of diseases such as cancer with enhanced selectivity for precision medicine.

Photoacoustic (PA) imaging, which relies on ultrasound signals generated by photothermal expansion of light-absorbing tissues or contrast probes under pulsed laser irradiation, has emerged as a promising type of biomedical imaging technique combining advantages of both optical and ultrasound imaging (10–12). Different from conventional fluorescence or bioluminescence imaging techniques that are suitable mostly for small animals, PA imaging has already moved into clinical trials owing to its significantly improved in vivo imaging depth (as deep as ~12 cm) and spatial resolution compared with traditional optical imaging modalities (10, 11, 13). A large variety of nanoscale agents, including both organic and inorganic ones, with absorption in the near-infrared (NIR) "tissue transparent" optical window have been extensively explored as PA imaging probes (14–20). For example, many types of nanoparticles with strong and constant NIR absorbance are often used for enhanced blood pool imaging and PA imaging of tumors (15, 16, 19). In addition, smart PA imaging nanoprobes with their absorbance spectra responsive to certain physiological signals such as reactive oxygen species (ROS), pH, and enzymes have also received substantial interest in recent years (12, 21, 22), because such a type of imaging would provide critical information directly related to disease progression and mechanisms. However, a sensitive and biocompatible nanoprobe that can precisely detect H_2O_2 in vivo by PA imaging has not yet been reported, to our best knowledge.

In this work, a liposomal nanocarrier simultaneously loaded with HRP and its substrate, 2,2′-azino-bis(3-ethylbenzothiazoline-6-sulfonic acid) (ABTS), is fabricated for in vivo H_2O_2 detection by PA imaging. The obtained Lipo@HRP&ABTS nanoprobe in the presence of H_2O_2 would show strong NIR absorbance owing

Significance

Hydrogen peroxide is closely associated with many important physiological and pathological events. Herein, we develop a liposomal nanoprobe for in vivo H_2O_2-responsive chromogenic assay, which is highly specific and sensitive to H_2O_2. Using such a nanoprobe, photoacoustic imaging of H_2O_2-related inflammation processes in mice induced by either LPS or bacteria is realized. Meanwhile, such a nanoprobe, by reacting with endogenous H_2O_2 produced by tumor cells, allows sensitive photoacoustic imaging of early-stage small tumors and orthotopic brain glioma and even enables accurate differentiation of metastatic sentinel lymph nodes from nonmetastatic ones. Furthermore, owing to its H_2O_2-responsive near-infrared absorbance, selective photothermal ablation of tumors is also achieved, illustrating the promise of using this nanoproble for tumor theranostics with great specificity.

Author contributions: Q.C., X.S., and Z.L. designed research; Q.C., C.L., X.S., J.C., Z.Y., H.Z., and L.F. performed research; Q.C. and Z.L. analyzed data; and Q.C. and Z.L. wrote the paper.

The authors declare no conflict of interest.

This article is a PNAS Direct Submission.

[1]To whom correspondence should be addressed. Email: zliu@suda.edu.cn.

This article contains supporting information online at www.pnas.org/lookup/suppl/doi:10.1073/pnas.1701976114/-/DCSupplemental.

to the HRP-catalyzed oxidization of colorless ABTS substrate into its green oxidized form, relying on a well-established chromogenic reaction extensively applied in bioanalysis techniques such as ELISA. Notably, such a nanoprobe is highly specific and sensitive to H_2O_2, with detection sensitivity down to the submicromolar level by PA imaging. Thus, using Lipo@HRP&ABTS nanoprobe, PA imaging of H_2O_2-related inflammation process is realized, revealing the development of inflammation induced by LPS or bacterial infection as well as the slowing down of inflammation after treatment by an antiinflammatory drug. In additional, such a Lipo@HRP&ABTS nanoprobe can also be used for in vivo PA imaging of s.c. tumors and orthotopic brain glioma upon systemic i.v. injection, or metastatic tumor cells within sentinel lymph nodes (SLNs), owing to the endogenous H_2O_2 production by tumor cells. Furthermore, using Lipo@HRP&ABTS accumulated in the tumor and its H_2O_2-induced NIR absorbance, tumor-specific photothermal ablation is successfully realized under NIR laser irradiation, which meanwhile induces minimal nonspecific heating to normal tissues without abnormal accumulation of H_2O_2. Our work achieves in vivo PA imaging of H_2O_2 using a liposomal optical nanoprobe, which is useful not only for in vivo detection of inflammations or tumors with great sensitivity but also for tumor-specific photothermal ablation with high efficacy and minimal nonspecific heating damage to normal tissues.

Results

Liposomes are spherical vesicles with a bilayer membrane structure usually composed by phospholipids and have been widely used for drug delivery owning to their versatile loading capacities for various types of drugs, excellent biocompatibility, and stealth-like long blood circulation behavior if appropriately modified (23). In this work, Lipo@HRP&ABTS liposomal nanoparticles were prepared according to the standard protocol. In brief, a mixture of 1,2-dihexadecanoyl-*sn*-glycero-3-phosphocholine (DPPC), cholesterol, and 1,2-distearoyl-*sn*-glycero-3-phosphoethanolamine-*N*-(amino-(polyethyleneglycol)-2000) (DSPE- PEG5000) at a molar ratio of 6.0:4.0:0.5 were used for the liposome formulation. ABTS with slight hydrophobicity can added during lipid membrane formation, whereas the hydrophilic HRP protein can be encapsulated into the aqueous core (Fig. 1*A*). Transmission electron microscopy (TEM) imaging indicated the successful formation of liposomal structure for the obtained Lipo@HRP&ABTS, which showed uniform spherical shape with an average diameter of ~100 nm (Fig. 1*B*), as further verified by dynamic light scattering measurement (Fig. 1*C*). The absorbance spectrum of Lipo@HRP&ABTS exhibited a characteristic absorption peak of ABTS at 342 nm, indicating the successful encapsulation of ABTS (Fig. S1). The loading capacities of ABTS and HRP were determined to be 23.17% and 5%, by UV-visible (UV-vis) absorbance spectra and bicinchoninic acid protein assay, respectively.

HRP has been extensively used in biochemistry applications such as ELISA, owing to its high efficiency to catalyze the conversion of chromogenic substrates such as 3′,5,5′-tetramethylbenzidine and ABTS into colored products (24). Because H_2O_2, with much lower polarity in comparison with H_2O, is able to transport through lipid bilayers (25), HRP loaded in liposomes could catalyze the oxidation of liposomal-loaded ABTS in the presence of environmental H_2O_2 into its oxidized form with a greenish color and strong optical absorption in NIR region (700–900 nm). In our system, the concentration of H_2O_2 should be far below that of ABTS. Thus, according a previous study (26), the oxidation of ABTS by H_2O_2 was catalyzed by HRP by the following reaction, with two oxidized ABTS radical cations generated from one H_2O_2 molecule:

$$\mathrm{ABTS} + 1/2\ \mathrm{H_2O_2} \rightarrow \mathrm{ABTS}\bullet^{+} + 1/2\mathrm{H_2O}.$$

The H_2O_2 specificity of this reaction was evaluated by incubating Lipo@HRP&ABTS or Lipo@ABTS with different

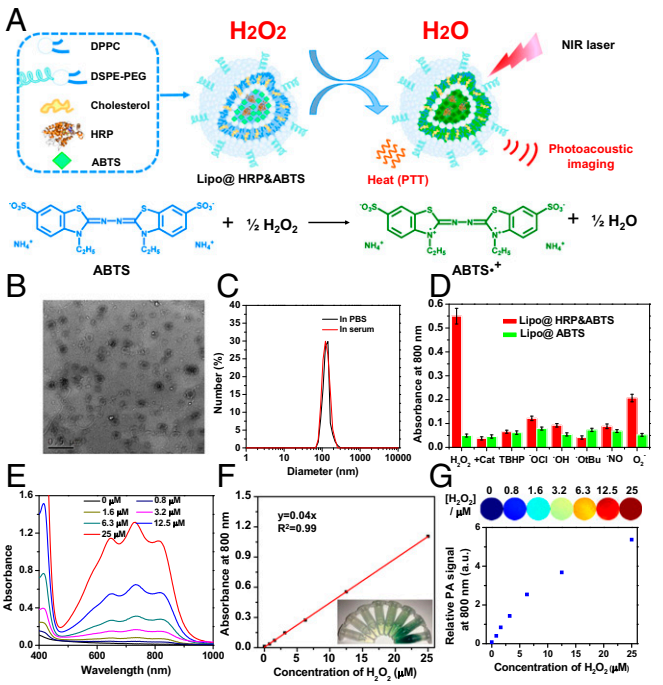

Fig. 1. Preparation and characterization of Lipo@HRP&ABTS nanoparticles. (*A*) A schematic illustration showing the formation of Lipo@HRP&ABTS and its applications in H_2O_2 detection by PA imaging and H_2O_2-activated photothermal therapy. (*B*) A TEM image of Lipo@HRP&ABTS. (*C*) Hydrodynamic diameters of Lipo@HRP&ABTS dispersed in PBS and serum. (*D*) Absorbance of Lipo@HRP&ABTS or Lipo@HRP&ABTS at 800 nm after incubation with various types of ROS (25 μM) for 30 min. H_2O_2 (25 μM) pretreated with Cat (0.2 mg/mL) was used as the negative control. (*E* and *F*) UV-vis–NIR absorbance spectra (*E*) and absorbance at 800 nm (*F*) of Lipo@HRP&ABTS (containing 0.069 mg/mL ABTS and 0.0148 mg/mL HRP) dispersed in buffers with different H_2O_2 concentrations. (*Inset*) A photo of those solutions. (*G*) PA images (*Top*) and PA signal intensities at 800 nm (*Bottom*) of Lipo@HRP&ABTS (containing 0.069 mg/mL ABTS and 0.0148 mg/mL HRP) dispersed in buffers with different H_2O_2 concentrations. Data are presented as the mean ± SEM.

types of ROS, including H_2O_2, tert-butyl hydroperoxide (TBHP), hypochlorite ($^{-}$OCl), hydroxyl radical ($^{\bullet}$OH), tert-butoxy radical ($^{\bullet}$OtBu), nitric oxide (NO$^{\bullet}$), and superoxide (O_2^{-}). It was found that Lipo@ABTS without HPR showed no appreciable response to all types of ROS. In contrast, Lipo@HRP&ABTS incubated with H_2O_2 showed obviously increased NIR absorbance, whereas there was no significant absorbance change when Lipo@HRP&ABTS was incubated with H_2O_2 pretreated by catalase (Cat) to trigger decomposition of H_2O_2, or other types of ROS except for superoxide, which induced a slight response for Lipo@HRP&ABTS (Fig. 1*D*). Notably, the response of Lipo@HRP&ABTS to superoxide (KO_2), a very strong oxidative agent, also seemed to be much weaker than that to H_2O_2 at the same concentration. Considering the rather low concentration of O_2^{-} within the in vivo environment compared with H_2O_2, our Lipo@HRP&ABTS could serve as a highly specific probe for detection of H_2O_2 in physiological environments.

Then, we carefully studied the H_2O_2-concentration-dependent absorbance change for Lipo@HRP&ABTS and the possibility of using PA imaging for H_2O_2 detection. The absorbance of Lipo@HRP&ABTS solutions at 800 nm increased in proportion to the concentrations of added H_2O_2 (Fig. 1 *E* and *F*). PA imaging of Lipo@ABTS&HRP incubated in solutions with different H_2O_2 concentrations was then carried out (Fig. 1*G*). As the H_2O_2 concentrations increased the detected PA signals of Lipo@ABTS&HRP at 800 nm showed a significant increase. Note that at high H_2O_2 concentrations the PA signals would exceed the linear range under our instrument setting. Notably, for

a solution with a rather low concentration of H_2O_2 at 0.8 μM, we could still detect a substantial level of PA signals from Lipo@HRP&ABTS, suggesting the great sensitivity of this nanoprobe for PA detection of H_2O_2 down to the submicromolar level. Therefore, such Lipo@ABTS&HRP can be used for the detection of H_2O_2 with high specificity and sensitivity.

Inflammation is a complex biological response of body tissues to harmful stimuli such as pathogens, damaged cells, or irritants and would produce a large amount of ROS, including superoxide anion, hydroxyl radical, and H_2O_2 (27). To demonstrate the potential of Lipo@HRP&ABTS for in vivo H_2O_2 detection, the inflammatory disease model was established via i.p. injection of LPSs (Fig. 2*A*), a lipoglycan that would cause in vivo inflammatory responses (28). For H_2O_2 detection during inflammation, mice 24 h after injection of LPS were then i.p. injected with Lipo@HRP&ABTS, with Lipo@ABTS used as the control. PA imaging was conducted thereafter to image the mouse abdomen. Interestingly, for mice with LPS-induced inflammation, rather strong PA signals appeared in the abdomen of mice after injection of Lipo@HRP&ABTS, but not for those with injection of Lipo@ABTS without HRP (Fig. 2 *B* and *C*). As another negative control, healthy mice without LPS pretreatment showed negligible PA signals after injection with Lipo@HRP&ABTS. Those results collectively demonstrate the possibility of using Lipo@HRP&ABTS for in vivo PA imaging of H_2O_2 resulting from inflammation. Considering that the PA signals in mice with inflammation reached their peak level 20–30 min after i.p. injection of Lipo@HRP&ABTS (Fig. 2*C*), we therefore chose 20 min (after injection of imaging probe) as the standard imaging time point for PA imaging-based inflammation detection in our system.

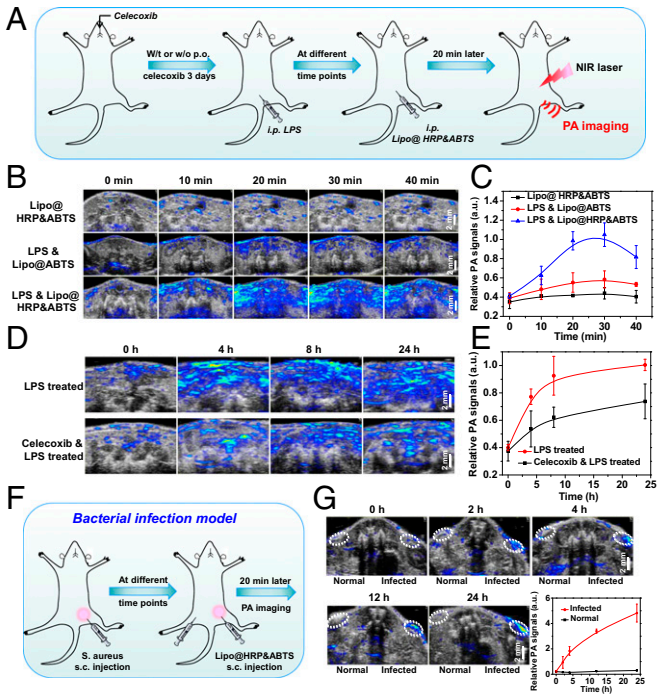

Fig. 2. PA imaging for in vivo inflammation detection with Lipo@HRP&ABTS. (*A*) Schematic illustration showing PA imaging of LPS-induced inflammation with Lipo@HRP&ABTS as the nanoprobe. Some of the mice were administrated per os (p.o.) with celecoxib at 3 d, 2 d, 1 d, and 2 h before LPS injection. At different time points after LPS injection, mice were i.p. injected with Lipo@HRP&ABTS for PA imaging. (*B*) In vivo PA images of mouse abdomen at 24 h after injection of LPS to induce inflammation with i.p. injection of Lipo@HRP&ABTS or Lipo@ABTS. (*C*) PA signals at 800 nm for mouse abdomen based on PA imaging data in *B*. (*D* and *E*) In vivo PA images (*D*) and PA signals at 800 nm (*E*) in mouse abdomen with or without oral feeding of celecoxib taken at different time points after i.p. injection of LPS. (*F*) Schematic illustration showing the detection of inflammation induced by bacteria with Lipo@HRP&ABTS by PA imaging. (*G*) In vivo PA images and PA signals at 800 nm of mice with bacterial infection after injection of Lipo@HRP&ABTS. The infected regions and normal regions with injection of Lipo@HRP&ABTS are highlighted in dashed circles. Three mice were measured in each group in *B*–*G*. Data are presented as the mean ± SEM.

Encouraged by the effective inflammation detection with Lipo@HRP&ABTS by PA imaging, then we wondered whether this nanoprobe could be used to track the development process of inflammation in mice. LPS was again used to provoke an acute inflammatory response in mice (Fig. 2*A*). To suppress the LPS-induced inflammation responses, celecoxib, a COX-2 selective nonsteroidal antiinflammatory drug, was used treat those animals by oral feeding for 3 d (20 $mg \cdot kg^{-1} \cdot d^{-1}$) before LPS treatment. At different time points after LPS injection, mice were i.p. injected with Lipo@HRP&ABTS (100 μL, containing 3.45 mg/mL ABTS and 0.74 mg/mL HRP) and imaged by a LAZR PA Imaging System 20 min later. As expected, the PA signals in the mouse abdomen gradually increased from 0 h to 24 h following injection of LPS (Fig. 2*D*). Quantification of PA signals further indicated gradually enhanced inflammation detected by the Lipo@HRP&ABTS (Fig. 2*E*). In contrast, for mice with pretreatment of celecoxib, the PA signals in the mouse abdomen following injection of LPS seemed to be obviously weaker (Fig. 2 *D* and *E*), suggesting that celecoxib would be able to suppress H_2O_2 generation resulted from LPS-induced inflammation.

To verify the ability of celecoxib to reduce inflammation, sera of mice after different treatments were collected at 6, 12, and 24 h following LPS treatment to analyze the changes of various cytokines including IL-1β, TNF-α, IL-12p40, and IL-6, which are important markers for inflammation-related immune responses. After LPS treatment we observed drastically elevated serum cytokine levels, which, however, seemed to be significantly reduced for mice pretreated with celecoxib, confirming the successful establishment of inflammation resulted from LPS treatment, as well as the effective antiinflammatory effect of celecoxib (Fig. S2). In addition, the average weights of mice treated with LPS showed significant decrease, whereas the LPS-induced weight decrease for mice pretreated with celecoxib was obviously relieved (Fig. S3), indicating the adverse LPS-triggered inflammation responses could be reduced by celecoxib treatment. Those results excellently correlate with our PA imaging data by using Lipo@HRP&ABTS for in vivo H_2O_2 detection and further verify that this imaging technique could be used for real-time monitoring of inflammation processes.

Different from LPS-induced inflammation, which is still an artificial inflammation model, bacterial infection is known to be able to trigger severe inflammation for the infected organs. During bacterial infection cells would undergo the enhanced oxidative stress and produce ROS, especially H_2O_2 (29). Thus, we want to use this nanoprobe to detect bacterial infection in mice by PA imaging. The bacterial infection model was established by s.c. injection of *Staphylococcus aureus* into healthy mice (Fig. 2*F*). Then, mice with *S. aureus*-infected s.c. abscesses, which was confirmed by the histological examination (Fig. S4), were locally injected with Lipo@HRP&ABTS for PA imaging. Excitingly, PA signals in the area with *S. aureus* infection significantly increased over time, whereas those in the uninfected area showed negligible changes after injection with Lipo@HRP&ABTS (Fig. 2*G*). Therefore, our Lipo@HRP&ABTS nanoprobe can successfully detect bacterial infection by PA imaging.

It is known that the tumor microenvironment is capable of controlling the proliferation of malignant cells, angiogenesis, metastasis, and subversion of adaptive immunity (30). During the growth of solid tumors inflammatory cells and fast-growing tumor cells would generate a substantial amount of H_2O_2 in the tumor microenvironment at concentrations of ~50–100 μM (31, 32).

Therefore, H_2O_2 detection based on our Lipo@HRP&ABTS by PA imaging may be a useful strategy for tumor diagnosis and prognosis. Similar to many other PEGylated liposomes, it was found that our Lipo@HRP&ABTS nanoprobe with fluorescent labeling after i.v. injection also showed prolonged blood circulation time and efficient tumor passive retention by the enhanced permeability and retention effect (33), as revealed by in vivo and ex vivo fluorescence imaging (Fig. S5). To study the potential of Lipo@HRP&ABTS for tumor detection, mice bearing s.c. murine breast 4T1 tumors were i.v. injected with Lipo@ABTS, Lipo@HRP, or Lipo@HRP&ABTS (200 μL, containing 3.45 mg/mL ABTS and 0.74 mg/mL HRP). After injection, mice were imaged by the Vevo LAZR Imaging System at different time points (Fig. 3*A*). Interestingly, the PA signals at 800 nm obviously increased over time in tumors of mice injected with Lipo@HRP&ABTS, whereas the tumors of mice injected with Lipo@ABTS or Lipo@HRP exhibited negligible PA signals (Fig. 3 *B* and *C*), despite similar levels of tumor retention for those liposomal nanoparticles. Considering that Lipo@HRP@ABTS within fresh mouse serum showed no significant response in terms of color change (Fig. S6), the observed PA signals in those tumors should be attributed to the existence of H_2O_2 in the tumor microenvironment.

Although there are well-established clinical imaging techniques for detection of tumors larger than 6–8 mm, accurate detection of very small tumors at their early stages remains a challenging task in the clinic (34). Encouraged by the highly sensitive H_2O_2 detection ability of Lipo@HRP&ABTS, we then tested the possibility of using this nanoprobe for imaging of tumors with rather small sizes. Lipo@HRP&ABTS (200 μL, containing 3.45 mg/mL ABTS and 0.74 mg/mL HRP) were i.v. injected into mice bearing 4T1 tumors at different stages (3, 5, and 7 d after inoculation) for PA imaging. Interestingly, the PA signals at 800 nm obviously increased over time even in small tumors with diameter at ∼2 mm (Fig. 3 *D* and *E*), demonstrating the capability of using our H_2O_2-responsive nanoprobe for imaging of tumors at very early stages.

Brain gliomas are the most aggressive neoplasms in the central nervous system (35). There are still difficulties in the early diagnosis and effective treatment of brain gliomas owing to the blood–brain barrier and the location of brain tumors that lie adjacent to or within anatomical structures (36). Therefore, there is an important need for noninvasive imaging of brain gliomas with high sensitivity. The orthotopic brain glioma model was created by injecting U87MG human glioma cells into the right brain of nude mice. At 10 d following tumor implantation the U87MG glioma-bearing mice were i.v. injected with Lipo@HRP&ABTS (Fig. 3*A*). The PA signals at 800 nm obviously increased over time in the right brain of mice, indicating the successful detection of such orthotopic glioma tumors inside the mouse brain in a noninvasive manner (Fig. 3 *F* and *G*).

Next, we would like to use this Lipo@HRP&ABTS nanoprobe for imaging of metastatic tumors, which would be responsible for most cases of cancer deaths. In many types of cancers (e.g., breast cancer and stomach cancer), cancer cells would first move along lymphatic vessels and form metastases at the SLNs, which are primary targets for early-stage tumor metastases (37, 38). Hence, it is of vital importance to identify early cancer metastasis on those lymph nodes for better treatment planning. Following a well-established protocol to create a lymph-node metastasis model (37, 39), 4T1 breast tumor cells were inoculated on the right hind footpad of mice. After ∼12 d, the lymph node in the inner knee of mice became touchable as a firm spherical lump, indicating SLN metastasis, which was also confirmed by the histological examination (Fig. S7). Then, those mice were injected with Lipo@HRP&ABTS (25 μL, containing 3.45 mg/mL ABTS and 0.74 mg/mL HRP) into their right legs with primary tumors on their footpads. For comparison, the same amount of Lipo@HRP&ABTS was injected into the left leg (without tumor inoculation) of the same mouse. In vivo PA imaging was then carried out (Fig. 3*H*). The PA signals at the lymph node with metastasis in the inner knee emerged rapidly and gradually enhanced after local injection of Lipo@HRP&ABTS. In contrast, no detectable PA signals showed up for nonmetastatic lymph nodes, although our liposomal nanoparticles showed effective retention in both healthy lymph nodes and metastatic nodes (Fig. S8). Our results suggest that PA imaging with the Lipo@HRP&ABTS nanoprobe would be able to accurately differentiate lymph nodes with metastatic tumors from those nonmetastatic ones based on their difference in H_2O_2 contents (Fig. 3 *I* and *J*), presenting an obvious advantage over conventional SLN-mapping techniques, which usually are not able to differentiate metastatic SLNs from normal nodes without metastases (40).

Considering that the NIR absorption of Lipo@HRP&ABTS would be significantly increased in the presence of H_2O_2 inside tumors, we suppose that this nanoprobe, apart from being used as a PA imaging probe, may serve as an H_2O_2-activated photothermal agent for in vivo tumor photothermal ablation. We first studied the photothermal effect of Lipo@HRP&ABTS dispersed in solutions with different H_2O_2 concentrations under the 808-nm NIR laser irradiation at the power density of 0.5 W/cm^2. With the same nanoparticle concentration, Lipo@HRP&ABTS showed obviously enhanced photothermal heating as H_2O_2 concentrations increased, indicating the strong H_2O_2 -dependent photothermal effect of Lipo@HRP&ABTS nanoparticles (Fig. S9). Then, the photothermal effect of Lipo@HRP&ABTS was studied in vivo. Mice bearing s.c. 4T1 tumors were i.v. injected with PBS, Lipo@ABTS, Lipo@HRP, or Lipo@HRP&ABTS (200 μL, containing 3.45 mg/mL ABTS and 0.74 mg/mL HRP). Twenty-four hours after injection, mice were irradiated by an 808-nm laser at a power density of ∼0.8 W/cm^2 for 10 min. An infrared

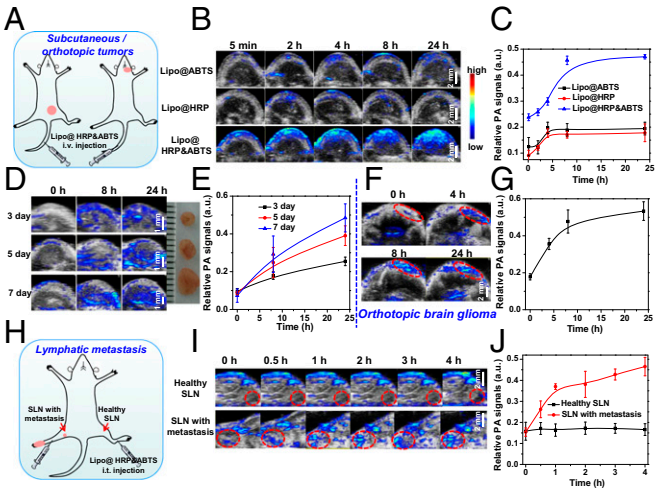

Fig. 3. PA imaging for in vivo tumor detection with Lipo@HRP&ABTS. (*A*) Schematic illustration of PA imaging on the s.c. tumor model and orthotopic brain glioma after i.v. injection of Lipo@HRP&ABTS. (*B*) In vivo PA images of 4T1 tumor-bearing mice taken at different time points after i.v. injection of Lipo@ABTS, Lipo@HRP, or Lipo@HRP&ABTS. (*C*) Relative PA signal intensities in tumors from different groups of mice at various time intervals based on PA imaging data shown in *B*. (*D*) In vivo PA images of mice bearing 4T1 tumors at different stages after i.v. injection of Lipo@HRP&ABTS. (*Inset*) A photo of these tumors. (*E*) Relative PA signal intensities in tumors at different stages based on PA imaging data shown in *D*. (*F* and *G*) In vivo PA images (*F*) and PA signals at 800 nm (*G*) in mice with orthotopic brain glioma tumors after i.v. injection of Lipo@HRP&ABTS. (*H*) Schematic illustration of PA imaging on the lymphatic metastasis tumor model. (*I*) In vivo PA images of SLNs with or without metastasis taken at different time points after injection of Lipo@HRP&ABTS. SLNs are highlighted by dashed circles in those images. (*J*) Relative PA signal intensities in SLNs at various time intervals based on PA imaging data shown in *I*. Three mice were measured in each group in *B*–*J*. Data are presented as the mean ± SEM.

thermal camera (Fotric 225) was used to monitor the temperature change on the tumor surface during the laser irradiation. For mice injected with Lipo@HRP&ABTS, their tumor surface temperature rapidly increased from ~34 °C to ~55 °C under the NIR laser. Conversely, the tumor temperature of mice injected with other control nanoparticles without the H_2O_2-dependent NIR absorbance under the same irradiation showed only slight changes (Fig. 4 *A* and *B*).

We then studied the treatment outcome of the photothermal therapy with such Lipo@HRP&ABTS nanoparticles in vivo. Mice bearing s.c. 4T1 tumors were randomly divided into three groups ($n = 5$ per group): PBS with light irradiation (810 nm, 0.8 W/cm^2 for 10 min, irradiated at 24 h postinjection), Lipo@HRP&ABTS without laser irradiation, and Lipo@HRP&ABTS with laser irradiation. Notably, tumors of mice treated by Lipo@HRP&ABTS and laser irradiation were effectively ablated (tumors were completely eliminated in four out of five mice). In marked contrast, neither the laser irradiation nor Lipo@HRP&ABTS injection alone affected the tumor growth (Fig. 4*D* and Fig. S10). H&E staining of tumor slices collected 1 d after various treatments further confirmed that cancer cells treated by Lipo@HRP&ABTS and laser irradiation were seriously damaged (Fig. 4*C*).

In addition to the s.c. tumor model, the photothermal effect of Lipo@HRP&ABTS was also evaluated on the lymphatic metastasis tumor model. Four hours after injection of Lipo@HRP&ABTS (25 μL, containing 3.45 mg/mL ABTS and 0.74 mg/mL HRP) into the footpads of mice with or without tumors, the lymph nodes of mice were exposed to the NIR laser (0.8 W/cm^2 for 5 min). The infrared thermal images indicated that the temperature on the lymph nodes with metastases rapidly increased, whereas the lymph nodes without metastasis under the same irradiation showed only a little change (Fig. 4 *E* and *F*). Based on our previous work, surgical removal of primary tumors together with photothermal ablation of metastatic SLNs would remarkably reduce chances of cancer metastases and prolong animal survival, offering significant benefit in cancer treatment (37, 39).

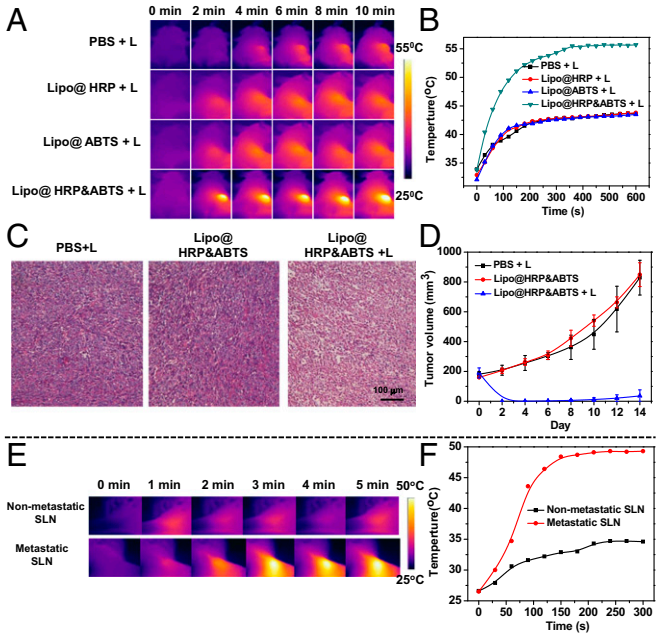

Fig. 4. In vivo photothermal therapy with Lipo@HRP&ABTS. (*A* and *B*) IR thermal images (*A*) and tumor temperature change curves (*B*) of 4T1 tumor-bearing mice after i.v. injection of Lipo@HRP, Lipo@ABTS, or Lipo@HRP&ABTS under the 808-nm laser irradiation (+L, 0.8 W/cm^2 for 10 min). (*C*) H&E-stained tumor slices collected from mice at the following day after different treatments. (*D*) The tumor growth curves of different groups of mice after various treatments indicated (five mice per group). (*E* and *F*) IR thermal images (*E*) and temperature changes (*F*) of SLNs without (upper row) or with (lower row) metastases on mice with local injection of Lipo@HRP&ABTS into mouse legs under 808-nm laser irradiation (0.8 W/cm^2 for 5 min).

Discussion

H_2O_2 is closely associated with a variety of physiological and pathological events in living organisms (4, 32). Thus, developing nanoprobes and imaging techniques for selective imaging of H_2O_2 would provide useful tools for better understanding of the occurrence and development of various diseases. In this study, HRP and its substrate ABTS are simultaneously loaded in liposomes as a unique nanoprobe to enable an in vivo chromogenic reaction for real-time PA imaging of H_2O_2. Such a technique with Lipo@HRP&ABTS is able to selectively detect H_2O_2 with sensitivity down to the submicromolar level. Compared with conventional H_2O_2 detection techniques based on fluorescence or bioluminescence imaging (3, 7, 8), PA imaging would offer remarkably improved imaging penetration depth to allow sensitive detection of H_2O_2 in deep tissues. Thus, an H_2O_2-related inflammation process induced by LPS or bacterial infection can be vividly observed under PA imaging using Lipo@HRP&ABTS, which may serve as a useful tool to accurately map out the inflammation/infection areas in the body and closely track such processes for better diagnosis and prognosis of infections.

In addition to the inflammation imaging, Lipo@HRP&ABTS is also demonstrated to be an effective PA imaging probe for tumors by responding to H_2O_2 in the tumor microenvironment. Early-stage tumors as small as 2 mm, as well as orthotopic brain gliomas, have been successfully imaged by our technique after systemic injection of this nanoproble. Such a technique may be particularly meaningful when used for mapping of metastatic SLNs. Although SLN mapping is an important step during surgical removal of several types of solid tumors, current SLN mapping methods by injecting dyes or carbon nanoparticles into primary tumors are not able to accurately differentiate metastatic SLNs from nonmetastatic ones, because both of them would show passive retention of those probes (37, 39). With our Lipo@HRP&ABTS nanoparticles injected near the primary tumor we would then be able to distinguish lymph nodes with metastatic tumors from those normal, nonmetastatic ones based on their differences in H_2O_2 contents by PA imaging.

Apart from its excellent H_2O_2 detection function, Lipo@HRP&ABTS has also been proven to be an H_2O_2-activated photothermal agent. Conventional photothermal agents would be heated up under laser irradiation if they are retained in normal tissues or organs, resulting in possible heat damage to those tissues during photothermal ablation of tumors. In contrast, with Lipo@HRP&ABTS nanoparticles tumors with high H_2O_2 contents would be effectively ablated but normal issues or organs without H_2O_2 up-regulation would not be heated even with retention of nanoparticles, offering obviously improved specificity in tumor ablation treatment.

In conclusion, a liposomal nanoprobe, Lipo@HRP&ABTS, has been successfully fabricated in our work for highly specific and sensitive H_2O_2 detection by in vivo chromogenic assay under PA imaging, which could be used to image the inflammation process induced by either LPS or bacterial infection. Meanwhile, Lipo@HRP&ABTS is also sensitive enough to react with endogenous H_2O_2 in the tumor microenvironment, even within early-stage small tumors or metastatic lymph nodes, enabling sensitive tumor imaging and accurate identification of metastatic SLNs. Furthermore, Lipo@HRP&ABTS with H_2O_2-responsive NIR absorbance also allows tumor-specific photothermal therapy. Therefore, this work presents a type of H_2O_2-responsive liposome-based nanoprobe with capabilities in both inflammation imaging and cancer theranostics, promising for future applications in different aspects of precision medicine.

Materials and Methods

Female BALB/c mice (6–8 wk of age) were purchased from Nanjing Peng Sheng Biological Technology Co., Ltd. and used under protocols approved by the Soochow University Laboratory Animal Center. To establish the peritoneal inflammation in mice, 100 μL (1 mg/mL) LPS was i.p. injected in each mouse. To form s.c. abscesses, *S. aureus* (5×10^6 cfu) was s.c. injected into the back of each mouse. To develop the s.c. tumor model, 1×10^6 4T1 murine breast cancer cells in 50 μL PBS were s.c. injected into the back of each mouse. The brain glioma model was created following the well-established method (41) by injecting 2.5×10^5 U87MG human glioma cells in 10 μL PBS into the right brain of each female nude mouse and used ∼10 d later. To create the lymph node metastasis tumor model, 1×10^6 4T1 cells suspended in 20 μL PBS were injected into the right hind footpad of each mouse. After ∼12 d, we chose mice with spherical firm lumps touchable in their inner knee for our experiments. Further experimental details can be found in *SI Materials and Methods*.

ACKNOWLEDGMENTS. This work was partially supported by the National Science and Technology Major Project of China Grant 2016YFA0201200, National Natural Science Foundation of China Grant 51525203, the Collaborative Innovation Center of Suzhou Nano Science and Technology, the "111 Project" from the Ministry of Education of China, and a project funded by the Priority Academic Program Development of Jiangsu Higher Education Institutions.

1. Bai J, Jiang X (2013) A facile one-pot synthesis of copper sulfide-decorated reduced graphene oxide composites for enhanced detecting of H2O2 in biological environments. *Anal Chem* 85:8095–8101.
2. Winterbourn CC (2008) Reconciling the chemistry and biology of reactive oxygen species. *Nat Chem Biol* 4:278–286.
3. Van de Bittner GC, Dubikovskaya EA, Bertozzi CR, Chang CJ (2010) In vivo imaging of hydrogen peroxide production in a murine tumor model with a chemoselective bioluminescent reporter. *Proc Natl Acad Sci USA* 107:21316–21321.
4. Finkel T, Serrano M, Blasco MA (2007) The common biology of cancer and ageing. *Nature* 448:767–774.
5. Deng Z, et al. (2016) Engineering intracellular delivery nanocarriers and nanoreactors from oxidation-responsive polymersomes via synchronized bilayer cross-linking and permeabilizing inside live cells. *J Am Chem Soc* 138:10452–10466.
6. Bandyopadhyay A, Gao J (2016) Iminoboronate-based peptide cyclization that responds to pH, oxidation, and small molecule modulators. *J Am Chem Soc* 138: 2098–2101.
7. Miller EW, Albers AE, Pralle A, Isacoff EY, Chang CJ (2005) Boronate-based fluorescent probes for imaging cellular hydrogen peroxide. *J Am Chem Soc* 127:16652–16659.
8. Chang MCY, Pralle A, Isacoff EY, Chang CJ (2004) A selective, cell-permeable optical probe for hydrogen peroxide in living cells. *J Am Chem Soc* 126:15392–15393.
9. Lee D, et al. (2007) In vivo imaging of hydrogen peroxide with chemiluminescent nanoparticles. *Nat Mater* 6:765–769.
10. Kim C, Favazza C, Wang LV (2010) In vivo photoacoustic tomography of chemicals: High-resolution functional and molecular optical imaging at new depths. *Chem Rev* 110:2756–2782.
11. Xu MH, Wang LHV (2006) Photoacoustic imaging in biomedicine. *Rev Sci Instrum* 77: 041101.
12. Chen Q, et al. (2015) A self-assembled albumin-based nanoprobe for in vivo ratiometric photoacoustic pH imaging. *Adv Mater* 27:6820–6827.
13. Zhou Y, et al. (2016) A phosphorus phthalocyanine formulation with intense absorbance at 1000 nm for deep optical imaging. *Theranostics* 6:688–697.
14. Cheng K, et al. (2014) Construction and validation of nano gold tripods for molecular imaging of living subjects. *J Am Chem Soc* 136:3560–3571.
15. Song KH, Kim C, Cobley CM, Xia Y, Wang LV (2009) Near-infrared gold nanocages as a new class of tracers for photoacoustic sentinel lymph node mapping on a rat model. *Nano Lett* 9:183–188.
16. Cheng L, et al. (2014) PEGylated WS(2) nanosheets as a multifunctional theranostic agent for in vivo dual-modal CT/photoacoustic imaging guided photothermal therapy. *Adv Mater* 26:1886–1893.
17. De la Zerda A, et al. (2008) Carbon nanotubes as photoacoustic molecular imaging agents in living mice. *Nat Nanotechnol* 3:557–562.
18. Kim JW, Galanzha EI, Shashkov EV, Moon HM, Zharov VP (2009) Golden carbon nanotubes as multimodal photoacoustic and photothermal high-contrast molecular agents. *Nat Nanotechnol* 4:688–694.
19. Liang XL, et al. (2015) PEGylated polypyrrole nanoparticles conjugating gadolinium chelates for dual-modal MRI/photoacoustic imaging guided photothermal therapy of cancer. *Adv Funct Mater* 25:1451–1462.
20. Li K, Liu B (2014) Polymer-encapsulated organic nanoparticles for fluorescence and photoacoustic imaging. *Chem Soc Rev* 43:6570–6597.
21. Dragulescu-Andrasi A, Kothapalli SR, Tikhomirov GA, Rao J, Gambhir SS (2013) Activatable oligomerizable imaging agents for photoacoustic imaging of furin-like activity in living subjects. *J Am Chem Soc* 135:11015–11022.
22. Pu K, et al. (2014) Semiconducting polymer nanoparticles as photoacoustic molecular imaging probes in living mice. *Nat Nanotechnol* 9:233–239.
23. Feng LZ, et al. (2016) Cisplatin-prodrug-constructed liposomes as a versatile theranostic nanoplatform for bimodal imaging guided combination cancer therapy. *Adv Funct Mater* 26:2207–2217.
24. Wei H, Wang E (2013) Nanomaterials with enzyme-like characteristics (nanozymes): Next-generation artificial enzymes. *Chem Soc Rev* 42:6060–6093.
25. Bienert GP, Schjoerring JK, Jahn TP (2006) Membrane transport of hydrogen peroxide. *Biochim Biophys Acta* 1758:994–1003.
26. Kadnikova EN, Kostić NM (2002) Oxidation of ABTS by hydrogen peroxide catalyzed by horseradish peroxidase encapsulated into sol–gel glass: Effects of glass matrix on reactivity. *J Mol Catal, B Enzym* 18:39–48.
27. Hansson GK (2005) Inflammation, atherosclerosis, and coronary artery disease. *N Engl J Med* 352:1685–1695.
28. Trent MS, Stead CM, Tran AX, Hankins JV (2006) Diversity of endotoxin and its impact on pathogenesis. *J Endotoxin Res* 12:205–223.
29. Korupalli C, et al. (2017) Acidity-triggered charge-convertible nanoparticles that can cause bacterium-specific aggregation in situ to enhance photothermal ablation of focal infection. *Biomaterials* 116:1–9.
30. Finger EC, Giaccia AJ (2010) Hypoxia, inflammation, and the tumor microenvironment in metastatic disease. *Cancer Metastasis Rev* 29:285–293.
31. Chen Q, et al. (2016) Intelligent albumin-MnO2 nanoparticles as pH-/H2 O2 -responsive dissociable nanocarriers to modulate tumor hypoxia for effective combination therapy. *Adv Mater* 28:7129–7136.
32. Szatrowski TP, Nathan CF (1991) Production of large amounts of hydrogen peroxide by human tumor cells. *Cancer Res* 51:794–798.
33. Torchilin VP (2005) Recent advances with liposomes as pharmaceutical carriers. *Nat Rev Drug Discov* 4:145–160.
34. Lyman GH, et al.; American Society of Clinical Oncology (2005) American Society of Clinical Oncology guideline recommendations for sentinel lymph node biopsy in early-stage breast cancer. *J Clin Oncol* 23:7703–7720.
35. Veiseh O, et al. (2009) Specific targeting of brain tumors with an optical/magnetic resonance imaging nanoprobe across the blood-brain barrier. *Cancer Res* 69: 6200–6207.
36. Galve-Roperh I, et al. (2000) Anti-tumoral action of cannabinoids: Involvement of sustained ceramide accumulation and extracellular signal-regulated kinase activation. *Nat Med* 6:313–319.
37. Chen Q, et al. (2014) An albumin-based theranostic nano-agent for dual-modal imaging guided photothermal therapy to inhibit lymphatic metastasis of cancer post surgery. *Biomaterials* 35:9355–9362.
38. Skobe M, et al. (2001) Induction of tumor lymphangiogenesis by VEGF-C promotes breast cancer metastasis. *Nat Med* 7:192–198.
39. Liang C, et al. (2014) Tumor metastasis inhibition by imaging-guided photothermal therapy with single-walled carbon nanotubes. *Adv Mater* 26:5646–5652.
40. Shangguan D, et al. (2006) Aptamers evolved from live cells as effective molecular probes for cancer study. *Proc Natl Acad Sci USA* 103:11838–11843.
41. Ruan S, et al. (2016) Increased gold nanoparticle retention in brain tumors by in situ enzyme-induced aggregation. *ACS Nano* 10:10086–10098.